

Transition of absolute instability from global to local modes in a gyrotron traveling-wave amplifier

T. H. Chang and N. C. Chen

Department of Physics, National Tsing Hua University, Hsinchu, Taiwan

Abstract

The gyrotron traveling-wave amplifier employing the distributed-loss scheme is capable of very high gain and effective in suppressing the global absolute instabilities. This study systematically characterizes the local absolute instabilities and their transitional behavior. The local absolute instabilities are analyzed using a model that incorporates the penetration of the field from the copper section into the lossy section. The axial modes were characterized from the perspective of beam-wave interaction and were found to share many characteristics with the global modes. The transition from global modes to local modes as the distributed loss increases was demonstrated. The electron transit angle in the copper section, which determines the feedback criterion, governs the survivability of an oscillation. In addition, the oscillation thresholds predicted using this model are more accurate than those obtained using a simplified model.

PACS number: 84.40.Ik, 84.40.Fe

I. INTRODUCTION

The gyrotron traveling-wave tube (gyro-TWT) amplifier featuring high power and broad bandwidth is an ideal source for advanced radar and communication applications, but the parasitic oscillations have for a long time hindered its realization [1-6]. Of these, oscillations associated with absolute instability are considered to be the most difficult [4,6,7]. As an example, Fig. 1 plots the $\omega - k_z$ diagram of a Ka-band gyro-TWT (whose parameters are listed in Table 1). The two parabolas represent the first two waveguide modes, and the two straight lines are the beam-wave synchronism lines of the first two cyclotron harmonics. Point 1 is the operating point of the gyro-TWT. Point 2, the intersection between the TE₂₁ mode curve and second synchronism line ($s=2$), locates potential self-oscillations. The intersection close to the cutoff frequency of the TE₂₁ mode has a small negative k_z . This backward-wave nature of the oscillation facilitates the field profile to be contracted at the beam entrance, which spoils the beam quality and destroys the amplification.

Among the several methods for effectively suppressing the absolute instabilities include the use of a drive signal [7,8], the use of sever/mode-selective circuit [9-14], and distributed-loss scheme [15-24]. The distributed-loss scheme has been studied for years and was demonstrated by the group at National Tsing Hua University (NTHU) in Taiwan [16,18,19]. They reported a zero-drive stability with a saturated power of 93 kW corresponding to an efficiency of 26.5% and an ultra-high gain of 70 dB [18,19]. In their experiment except for the distributed loss, a sufficiently

short copper section was required to suppress some oscillation formed in the copper section [18-20,22,23]. The oscillation thresholds are estimated using an effective length of the copper section [25-28]. However, such a simplified model fails to account for the penetration of the field into the lossy section, and so inaccurately predicts the starting current of the oscillation.

By using a complete distributed loss configuration, this study theoretically confirms the existence of the absolute instability, which is localized in the copper section. The axial modes of the local absolute instability are characterized in terms of the field profile, the energy deposition rate, and the electron transit angle. The effect of localization is illustrated. In addition, the transitions from global to local modes are demonstrated and discussed.

II. CHARACTERIZING LOCAL ABSOLUTE INSTABILITY

The following calculation employs a verified, single-mode, particle tracing code [18,19]. The simulation parameters, listed in Table I, are basically the same as those of the NTHU's gyro-TWT. The interaction circuit consists of a lossy section of length L_1 and resistivity ρ , followed by a copper section of length L_2 . A 2-cm loss taper is adopted at the interface between the lossy and the copper sections. Both sections are assumed to have a constant radius of 0.266 cm. The interaction structure is immersed in a uniform magnetic field. The variables L_1 , L_2 , and ρ are changed one at a time to study the localization property.

A. Localization of fields

Figure 2 shows the field profiles (solid curves) and energy deposition rates (dashed curves) of the first four local axial modes at their respective starting currents. The length of the lossy section L_1 is 15 cm and the length of the copper section L_2 is 10 cm. The resistivity of the lossy section is 50000 times that of the copper section ($\rho=50000 \rho_{\text{cu}}$). As shown in Fig. 2, the bulk field and energy deposition rate are located at the copper section. A recent investigation [29] showed that the number of the positive energy deposition regions determines the index of the global axial mode. The fundamental axial mode has only one positive energy deposition region and the second axial mode has two, and so on. The rule for the global modes seems to be applicable to the local modes and is used to identify the axial modes of the local absolute instability.

The field cannot be immediately damped to zero at the interface between the lossy section and the copper section. Hence, the field still penetrates the lossy section, slightly deforming field profiles. In addition, the reflective wave caused by circuit mismatch is responsible for the fluctuation in the field profile. The lower order mode generally corresponds to a higher reflection because the oscillation frequency is close to the waveguide cutoff. As shown in Fig. 2, the field and the energy deposition profiles of the fundamental mode fluctuate much greater than those of the other high-order modes.

B. Effective electron transit angle

Figure 3 plots the effective electron transit angle versus the copper section length L_2 for the first four local axial modes, where $L_1=15$ cm and $\rho=50000 \rho_{\text{cu}}$. The effective electron transit

angle Θ_{eff} is defined as

$$\Theta_{\text{eff}} \equiv (\omega - k_z v_z - \Omega_c) \tau, \quad (1)$$

where ω is the wave frequency; k_z is the wave propagation constant, and Ω_c is the relativistic electron cyclotron frequency. Notably, $\tau (= L_2 / v_{z0})$ is the time that the electron transits the copper section L_2 at the initial velocity v_{z0} . Θ_{eff} is the total wave phase variation observed by the electron in traversing the interaction space. Figure 3 shows that Θ_{eff} of the first four local axial modes remain in their respective optimum conditions, each separated by 2π ,

$$\Theta_{\text{eff},\ell} \approx (2\ell - 1)\pi, \quad \ell = 1, 2, 3, \dots, \quad (2)$$

where ℓ is the index of the local axial mode.

Interestingly, the bulk field gradually moves to the copper section as L_2 increases. Thus the effective electron transit angle Θ_{eff} approaches the optimum condition. The field profile, the energy deposition rate, and the electron transit angle manifest that the definition of the local axial modes is similar to that of the global axial modes. Although the local and global modes share many characteristics, they exhibit dramatically different properties as the distributed loss increases.

C. Oscillation thresholds insensitive to the loss properties

Figures 4(a) and 4(b) plot the start-oscillation currents against the applied loss ρ and the lossy section length L_1 , respectively. Figure 4(a) shows I_{st} versus ρ for the first four local axial modes with $L_1=15$ cm and $L_2=10$ cm. As the applied loss increases, the starting currents increase as

expected. However, unlike the global absolute instabilities, the starting current does not increase monotonously with the applied loss. The starting current of each local axial mode gradually converges to a specific value. This situation differs fundamentally from that of the global axial modes [18,19]. At sufficiently high resistivity the starting currents are insensitive to the applied loss, implying that the oscillations are localized in the copper section.

Figure 4(a) reveals that a higher axial mode corresponds to a better suppression ratio R , which is defined as

$$R \equiv \frac{I_{st}(\rho = 50000\rho_{cu})}{I_{st}(\rho = \rho_{cu})} . \quad (3)$$

The suppression ratios R for the first four axial modes are 2.05, 3.33, 4.26, and 6.17, respectively.

The ratios increase with the index of the local axial modes. A higher axial mode corresponds to a greater propagation constant k_z , indicating that a greater field will penetrate the lossy section. In that case, the distributed loss absorbs the backward propagating wave and cuts off the feedback mechanism, leading to the increase of the starting current. This property, first discovered in the transverse modes of absolute instabilities [23], is now applicable to the local axial modes.

Figure 4(b) plots the start oscillation current I_{st} versus the length of the lossy section L_1 with $L_2=10$ cm and $\rho=50000\rho_{cu}$. The starting current of each local axial mode is almost independent of the length of the lossy section. When a mode is fully localized at sufficient loss, it is insensitive to the lossy properties as verified in Figs. 4(a) and 4(b).

III. TRANSITION FROM GLOBAL MODE TO LOCAL MODE

The absolute instabilities are classified into global mode and local mode. The field profile of global absolute instability covers the entire interaction structure, whereas that of the local absolute instability is localized in the copper section. The similar characteristics of global and local modes enable us to examine how the global modes and local modes are related.

A. Criterion of the global-local mode transition

Figure 5(a) plots the starting currents of the first four axial modes as a function of the wall resistivity ρ with $L_1=15$ cm and $L_2=4.5$ cm. When the wall resistivity equals the resistivity of copper ($\rho = \rho_{\text{cu}}$), four global axial modes are well defined. As ρ is increased, all the start-oscillation currents raise – especially those of the fundamental, second, and fourth axial modes. A higher wall resistivity results in a higher oscillation threshold, as is already known. Surprisingly however, the loss cannot suppress the third global axial mode in this configuration. The starting current of the third axial mode increases gently, unlike those of the other three axial modes. The axial modes, which can be suppressed by the loss are global oscillations in nature, whereas the oscillations that are insensitive to the loss turn into the local modes.

The bulk fields of the local axial modes are concentrated in the copper section. It is therefore insensitive to the distributed loss. However, the start-oscillation currents of the local axial modes still rise slightly with the wall resistivity, because of the residue field in the lossy section. Increasing the wall resistivity shortens the effective copper length and the shortest length is equal to

L_2 . Hence the starting current slowly approaches the starting current of L_2 (8.84 A).

The effective electron transit angle Θ_{eff} characterizing the local axial modes could be used to determine the criterion of the global-local mode transition. Figure 5(b) plots the effective electron transit angle Θ_{eff} versus the wall resistivity ρ . The effective electron transit angle is the transit angle in the copper section (L_2) as defined in Eq. (1). It is expected that when an oscillation is fully localized in L_2 , Θ_{eff} should approach the optimal transit angle of π as defined in Eq. (2). It is interesting to note that the third global mode (at $\rho = \rho_{\text{cu}}$) has a Θ_{eff} close to π . Therefore, this mode always maintains an optimal feedback condition during the transitional process. This explains why the third global mode survives the heavy loss and transforms into the fundamental local mode. Based on the observation and a reasonable inference, the criterion of the global-local mode transition is

$$\Theta_{\text{eff}}(n \rightarrow \ell) \approx (2\ell - 1)\pi, \quad \ell = 1, 2, 3, \dots, \quad (4)$$

where n is the index of the global axial mode and ℓ is the index of the local axial mode.

Equation (4) is an empirical equation. It helps us to predict which global mode turns into a fully localized mode, but the extent of localization varies with the applied loss and oscillation frequency. For example, the second local mode is difficult to be fully localized due to higher k_z . The field penetrates into the lossy section resulting in slightly different optimal electron transit angle. However, for all practical purposes, the fundamental local mode is the principal concern, so Eq. (4) serves as a criterion of the global-local transition.

B. Transitional process

Figure 6 shows the transition from the third global mode to the fundamental local mode. The field profiles and energy deposition rates for four wall resistivities are display in Figs 6(a) and 6(b), respectively. Increasing the wall resistivity strongly dampens the field within the lossy section such that eventually only the field at the copper section remains. The energy deposition rates (Fig. 6(b)) provide an insight into the beam-wave interaction. The profiles of the energy deposition rates slightly change, but the amplitude decreases as the applied loss increases. At up to $\rho = 50000 \rho_{cu}$, the first two crests and troughs approach zero indicating that the beam-wave interaction in the lossy section is very small. The remaining field is fully located in the copper section.

Although the bulk fields of the third and fourth global axial modes are located in the copper section, only the field of the third axial mode in the copper section meets the optimal electron transit angle and survives the heavy losses. This implies, when dealing with a mode transition, the electron transit angle in the copper section is more essential than the field profile.

Figure 7 shows the transition of the second local mode from the sixth global mode. The field profiles and energy deposition rates for four resistivities are displayed in Figs 7(a) and 7(b), respectively. Increasing the wall resistivity dampens the field within the lossy section, but it is not as effective as the loss to the fundamental local mode. The bulk fields of the third, fourth, fifth, and sixth global axial modes are located in the copper sections, but only the third and sixth global modes turn into fundamental and second local modes. This suggests that the configuration plays a

role and will be discussed in the following section.

C. Role of configuration

Figure 8 shows transitions from the third, fourth, and fifth global modes to the fundamental local mode. The lossy section lengths L_1 are 16, 22, and 28 cm and L_2 is fixed at 4.5 cm. When the whole interaction section (L_1+L_2) is of copper, the global modes are well-defined (gray curves). With a loss of $50000 \rho_{\text{cu}}$, the global mode in each configuration transitions into the fundamental local modes (black curves). One might expect that with another 6 cm, i.e. $L_1=34$ cm, the next transition occurs, but in fact it is still the fifth global mode that transits to the fundamental local mode. Such incorrect inference is because the field penetrating ability k_z and the guide wavelength λ_g are varied with the oscillation frequency.

The behavior of an oscillation fully localized in the copper section is not correlated with the properties of the lossy section. Increasing the length of the lossy section just pushes the field profile downstream without changing its oscillation properties. This means no matter how we change L_1 it will transition to the fundamental local mode at sufficient loss. The configuration just provides a rough estimate of what transition will occur.

Figure 9(a) plots the starting currents I_{st} versus the copper section length L_2 for the first two local modes. The solid lines are obtained using a complete model (this work) and the dashed lines are obtained using a simplified model. The simplified model uses an effective length. Here we assume it equals L_2 . Both simulations employ a fixed L_1 of 15 cm. Regardless of the change in the

configuration L_2 , the starting currents can always be obtained, which fact again verifies that the length ratio between L_2 and L_1 is not critical in determining the survivability of an oscillation.

Figure 9(b) plots the effective electron transit angle Θ_{eff} versus the copper section length L_2 . The Θ_{eff} approaches the optimal values of π and 3π as mentioned in Eq. (2). The solid lines and the dashed lines represent the results of the complete model and those of the simplified model, respectively. As L_2 is shortened, the starting currents significantly increase, so is the oscillation frequencies. This explains why the simplified mode predicts a slightly higher electron transit angle. In the meantime, the complete model shows an opposite trend. Shorter L_2 corresponds to a higher k_z , which means the field will penetrate into the lossy section resulting in a decrease of the effective electron transit angle.

Figures 9(a) and 9(b) show that the two models are almost equivalent at long L_2 . However, at short L_2 , which is of practical interest, the predicted values differ greatly. For example, at $L_2=4.5$, the simplified model predicts a starting current of 8.84 A, while the present model predicts a value of 5.08 A. Obtaining an appropriate critical length for the simplified model is difficult since the field penetration effect varies with the oscillation frequency. Therefore, the simplified model cannot accurately determine the oscillation threshold, but this model can provide a more realistic result.

IV. CONCLUSION

This work presented a complete characterization of the local absolute instabilities and

discussed the transitions from global to local modes. The bulk field of the localized oscillation resides in the downstream copper section. Thus these local modes are virtually insensitive to the distributed loss, in sharp contrast to the global modes. The transitions from global to local modes reveal that the oscillation with an appropriate electron transit angle survives when a heavy loss is applied. The electron transit angle governs the survivability of the oscillation, rather than the field profile or the configuration.

At a large drive power, the amplifying wave suppresses the downstream local oscillation. Hence at saturated and low-gain operation, such a localized oscillation might not be detected. However, when a high-gain gyro-TWT is operated, the existence of such a localized oscillation spoils the linear region. Therefore, the complete model is needed to accurately evaluate the oscillation threshold in a zero-drive stable, high-gain gyro-TWT.

ACKNOWLEDGMENTS

The authors are grateful to Prof. K. R. Chu, Prof. S. H. Chen, and Prof. Y. S. Yeh for many helpful discussions. This work is sponsored by the National Science Council of Taiwan.

V. REFERENCES

- [1] J. A. Davies, Phys. Fluids **B 1**, 663 (1989).
- [2] V. L. Granastein, B. Levush, B. G. Danly, and R. K. Parker, IEEE Trans. Plasma Sci. **25**, 1322

(1997).

- [3] S. H. Gold and G. S. Nusinovich, *Rev. Sci. Instrum.* **68**, 3945 (1997).
- [4] K. R. Chu, *IEEE Trans. Plasma Sci.* **30**, 903 (2002).
- [5] G. S. Nusinovich, *Introduction to the Physics of Gyrotrons* (John Hopkins, Baltimore and London, 2004), Chap.6 and 7.
- [6] K. R. Chu, *Rev. Mod. Phys.* **76**, 489 (2004).
- [7] L. R. Barnett, L. H. Chang, H. Y. Chen, K. R. Chu, W. K. Lau, and C. C. Tu, *Phys. Rev. Lett.* **63**, 1062 (1989).
- [8] A. T. Lin and C. C. Lin, *Phys. Fluids B* **1**, 2286 (1989).
- [9] Q. S. Wang, D. B. McDermott, and N. C. Luhmann, Jr., *Phys. Rev. Lett.* **75**, 4322 (1995).
- [10] C. K. Chong, D. B. McDermott, and N. C. Luhmann, Jr., *IEEE Trans. Plasma Sci.* **26**, 500 (1998).
- [11] J. R. Sirigiri, M. A. Shapiro, and R. J. Temkin, *Phys. Rev. Lett.* **90**, 258302 (2003).
- [12] Y. S. Yeh, T. S. Wu, Y. T. Lo, C. W. Su, and S. C. Wu, *Int. J. Electronics*, **90**, 517 (2003).
- [13] G. S. Park, J. J. Choi, S. Y. Park, C. M. Armstrong, A. K. Ganguly, R. H. Kyser, and R. K. Parker, *Phys. Rev. Lett.* **74**, 2399 (1995).
- [14] J. Rodgers, H. Guo, G. S. Nusinovich, V. L. Granatstein, *IEEE Trans. Electron Devices.* **48**, 2434 (2001).
- [15] Y. Y. Lau, K. R. Chu, L. R. Barnett, and V. L. Granatstein, *Int. J. Infrared Millim. Waves* **2**,

395 (1981).

- [16] K. R. Chu, L. R. Barnett, H. Y. Chen, S. H. Chen, Ch. Wang, Y. S. Yeh, Y. C. Tsai, T. T. Yang, and T. Y. Dawn, *Phys. Rev. Lett.* **74**, 1103 (1995).
- [17] K. R. Chu, H. Guo, and V. L. Granatstein, *Phys. Rev. Lett.* **78**, 4661 (1997).
- [18] K. R. Chu, H. Y. Chen, C. L. Hung, T. H. Chang, L. R. Barnett, S. H. Chen, and T. T. Yang, *Phys. Rev. Lett.* **81**, 4760 (1998).
- [19] K. R. Chu, H. Y. Chen, C. L. Hung, T. H. Chang, L. R. Barnett, S. H. Chen, T. T. Yang, and D. Dialetis, *IEEE Trans. Plasma. Sci.* **27**, 391 (1999).
- [20] B. McDermott, H. H. Song, Y. Hirata, A. T. Lin, T. H. Chang, H. L. Hsu, P. S. Marandos, J. S. Lee, K. R. Chu, and N.C. Luhmann, Jr., *IEEE Trans. Plasma Sci.* **30**, 894 (2002).
- [21] M. Garven, J. P. Calame, B. G. Danly, K. T. Nguyen, B. Levush, F. N. Wood, and D. E. Pershing, *IEEE Trans. Plasma Sci.* **30**, 885 (2002).
- [22] H. H. Song, D. B. McDermott, Y. Hirata, L. R. Barnett, C. W. Domier, H. L. Hsu, T. H. Chang, W. C. Tsai, K. R. Chu, and N. C. Luhmann, Jr., *Physics Plasmas*, **11**, 2935 (2004).
- [23] W. C. Tasi, T. H. Chang, N. C. Chen, K. R. Chu, H. H. Song, and N. C. Luhmann, Jr., *Phys. Rev. E.* **70**, 056402 (2004).
- [24] Y. S. Yeh, Y. Y. Shin, Y. C. You, and L. K. Chen, *Phys. Plasmas*, **12**, 043108 (2005).
- [25] K. C. Leou, D. B. McDermott, A. J. Balkcum, N. C. Luhmann, Jr., *IEEE Trans. Plasma Sci.*, **22**, 585 (1994).

- [26] Q. S. Wang, D. B. McDermott, and N. C. Luhmann, Jr., Phys. Rev. Lett. **75**, 4322 (1995).
- [27] G. S. Nusinovich, O. V. Sinitsyn, and A. Kesar, Phys. Plasmas, **8**, 3427 (2001).
- [28] D. B. McDermott, H. H. Song, Y. Hirita, A. T. Lin, L.R. Barnett, T. H. Chang, H. L. Hsu, P. S. Marandos, J. S. Lee, K. R. Chu, and N. C. Luhmann, IEEE Trans. Plasma Sci., **30**, 894 (2002).
- [29] S. H. Chen, T. H. Chang, K. F. Pao, C. T. Fan, and K. R. Chu, Phys. Rev. Lett. **89**, 268303 (2002).

TABLE I. Simulation parameters.

Amplification mode	TE ₁₁ (s=1)
Oscillation mode	TE ₂₁ (s=2)
Cyclotron harmonic	Fundamental
Waveguide radius (r_w)	0.266 cm
Cutoff frequency	33.0 GHz
Beam voltage (V_b)	100 kV
Beam current (I_b)	3 A
Velocity ratio (v_{\perp}/v_z)	0.85
Velocity spread ($\Delta v_z/v_z$)	0%
Guiding center position (r_c)	0.35 r_w
Applied magnetic field (B_0)	12.54 kG
Lossy section length (L_1)	12-22 cm
Copper section length (L_2)	4.5-20 cm
Wall resistivity (ρ)	1-50000 ρ_{cu}

FIG.1 $\omega - k_z$ diagrams of the waveguide modes and the beam wave synchronism lines for a TE₁₁ mode, 34-GHz gyro-TWT, operating at the fundamental cyclotron harmonic.

FIG. 2 Field profile (solid lines) and energy deposition rate (dashed lines) of first four local axial modes with $L_1=15$ cm, $L_2=10$ cm, and $\rho=50000\rho_{\text{cu}}$.

FIG. 3 Effective electron transit angle Θ_{eff} versus copper section length L_2 for the first four local axial modes with L_1 and ρ as in Fig. 2.

FIG. 4 Start-oscillation current I_{st} versus (a) wall resistivity ρ and (b) lossy section length L_1 for first four local axial modes with L_2 and ρ as in Fig. 2.

FIG. 5 (a) Start-oscillation currents I_{st} and (b) effective electron transit angle Θ_{eff} of the first four modes versus the wall resistivity ρ with $L_1=15$ cm and $L_2=4.5$ cm. The starting currents increase with ρ , but the behavior of the third global axial mode differs greatly from those of the other modes.

FIG. 6 The third global mode transforms into the fundamental local mode as the wall resistivity increases. (a) Normalized field profile and (b) normalized energy deposition rate for different wall resistivities ρ with L_1 and L_2 as in Fig. 5.

FIG. 7 The sixth global mode is transformed into the second local mode as the wall resistivity increases. (a) Normalized field profile and (b) normalized energy deposition rate for different wall resistivities ρ with L_1 and L_2 as in Fig. 5.

FIG. 8 The third, fourth, and fifth global modes are transformed into the fundamental local mode

for three configurations. The lengths of the lossy section lengths L_1 are 16, 22, and 28 cm and L_2 is fixed at 4.5 cm. The gray curves are the field profiles with bare waveguide ($\rho = \rho_{\text{cu}}$) and the black lines are the field profiles obtained using heavy loss scheme ($\rho = 50000\rho_{\text{cu}}$).

FIG. 9 (a) Starting current I_{st} and (b) effective electron transit angle Θ_{eff} versus the length of the copper section L_2 for the first two local modes. The solid lines and the dashed lines are obtained using the complete model and the simplified model, respectively.

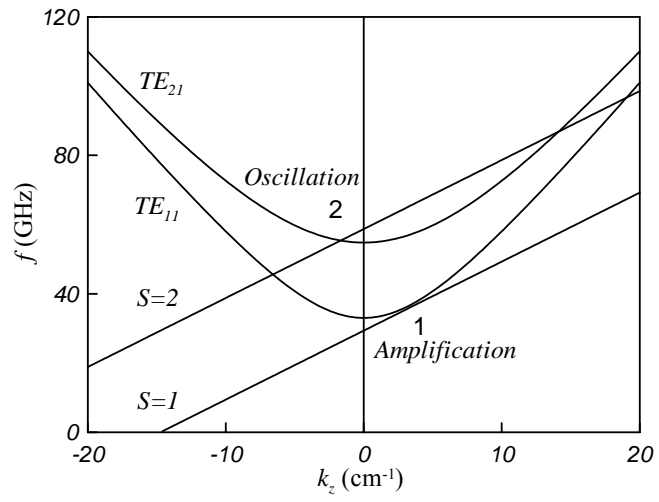


Fig. 1

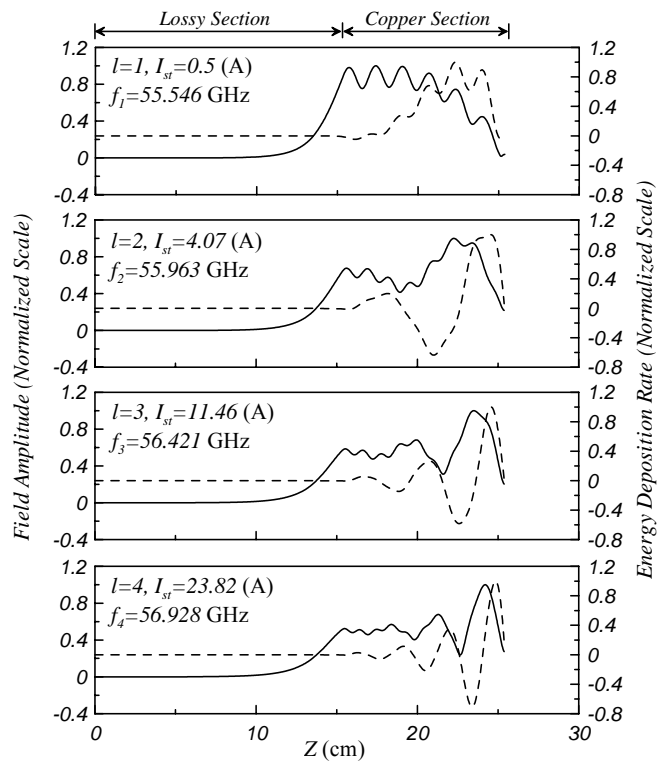


Fig. 2

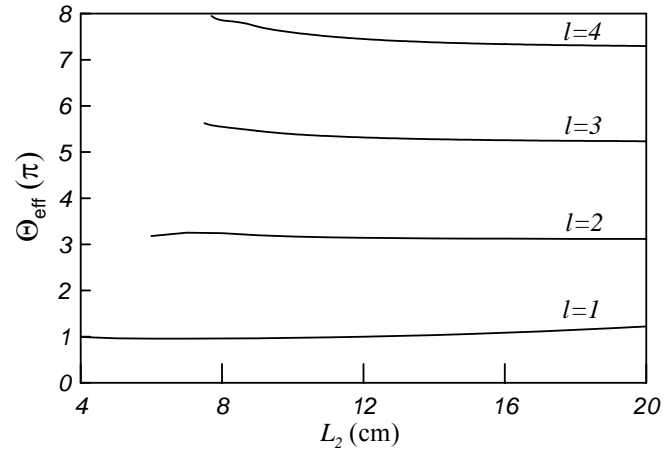


Fig. 3

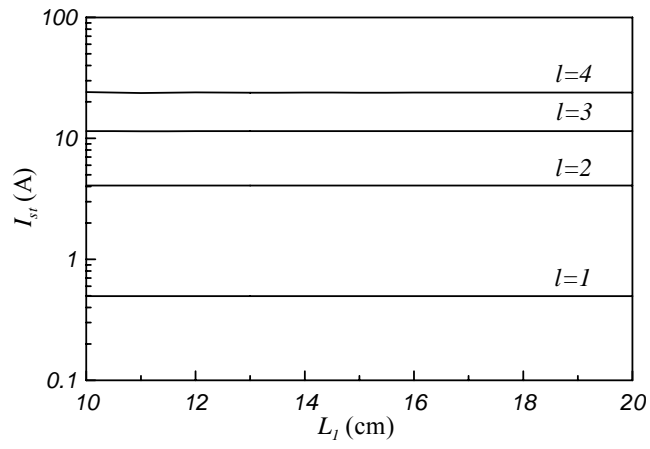
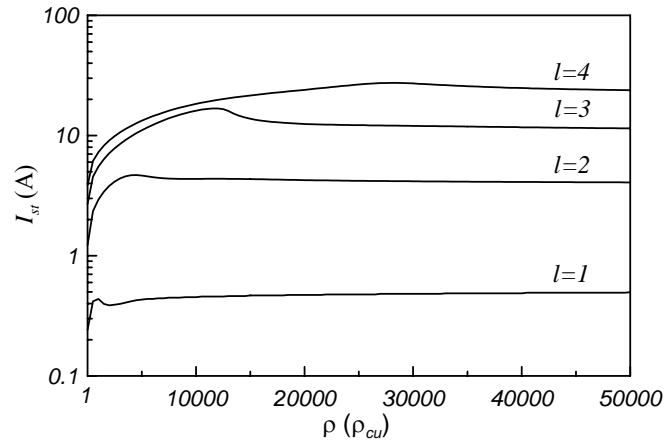


Fig. 4

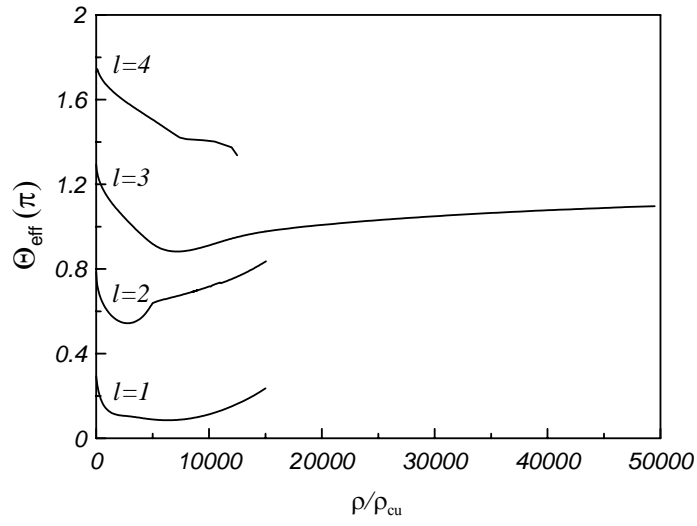
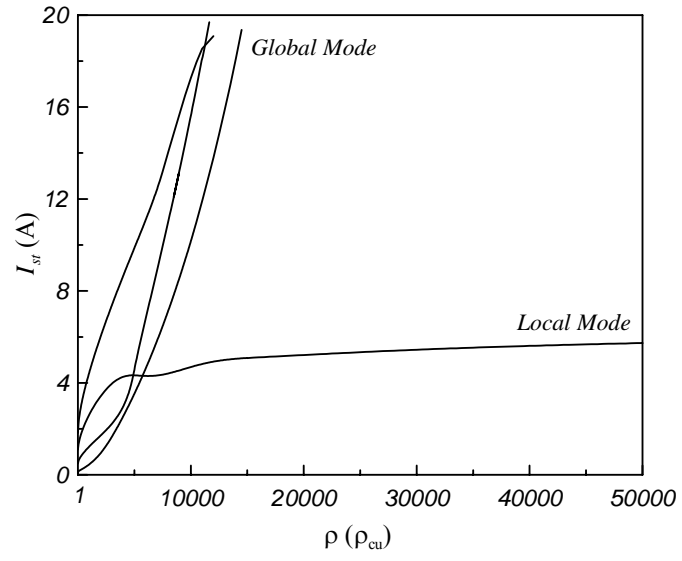


Fig. 5

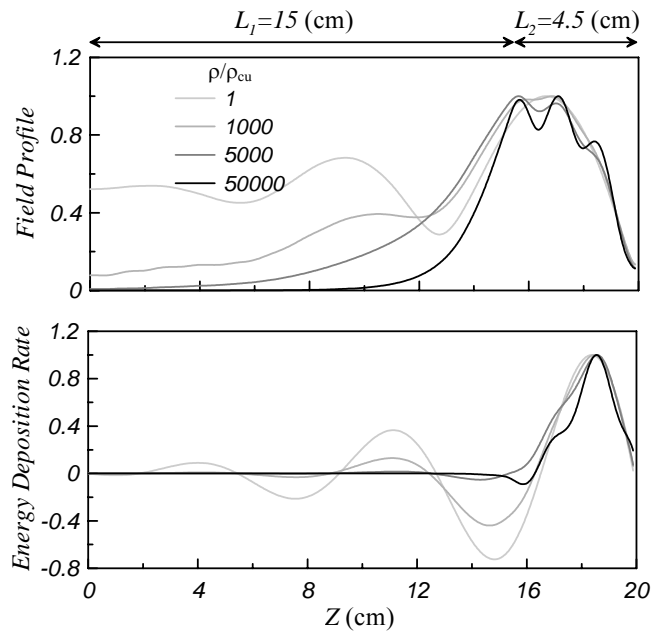


Fig. 6

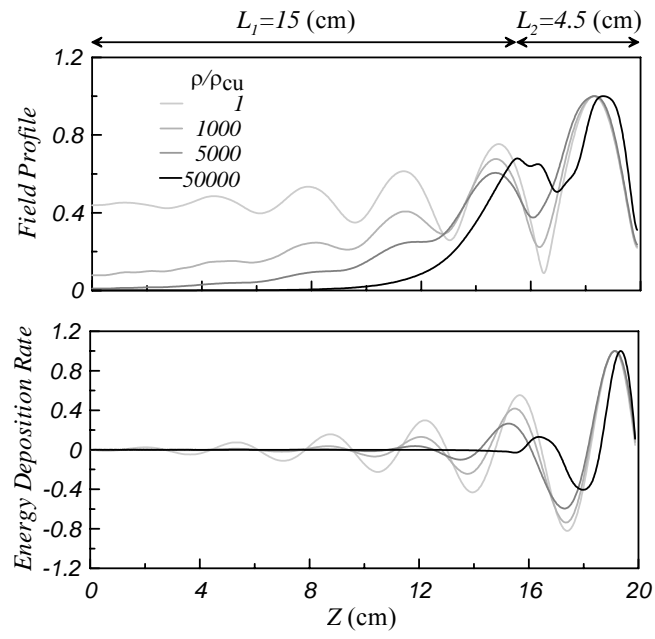


Fig. 7

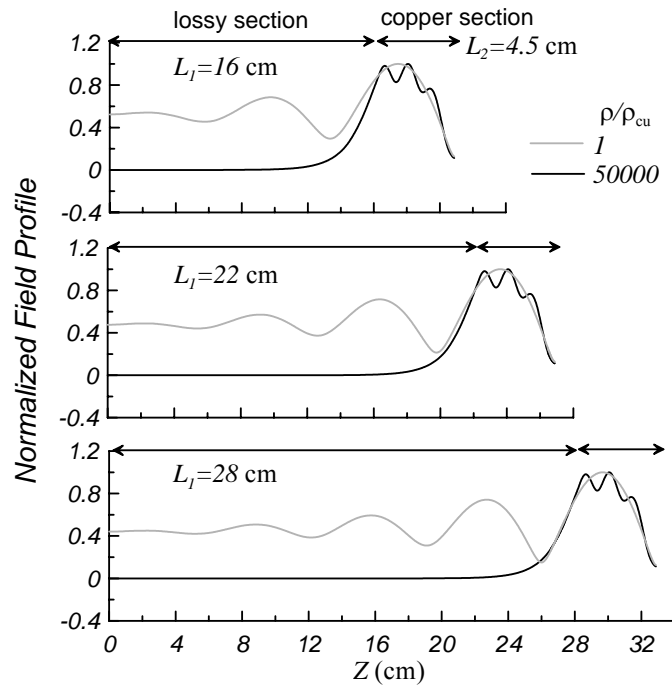


Fig. 8

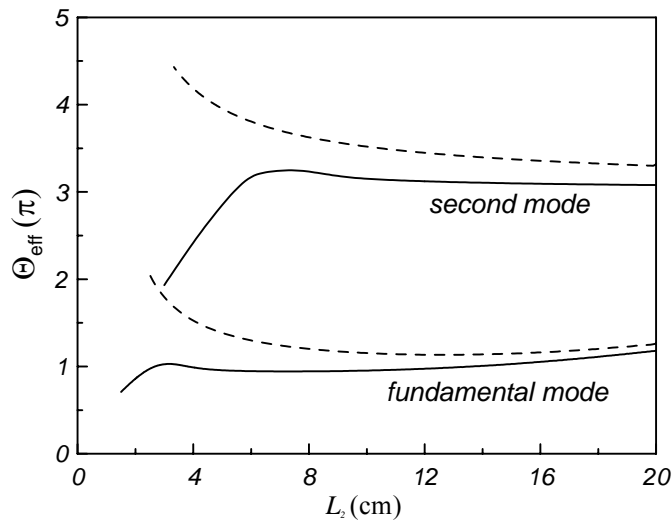
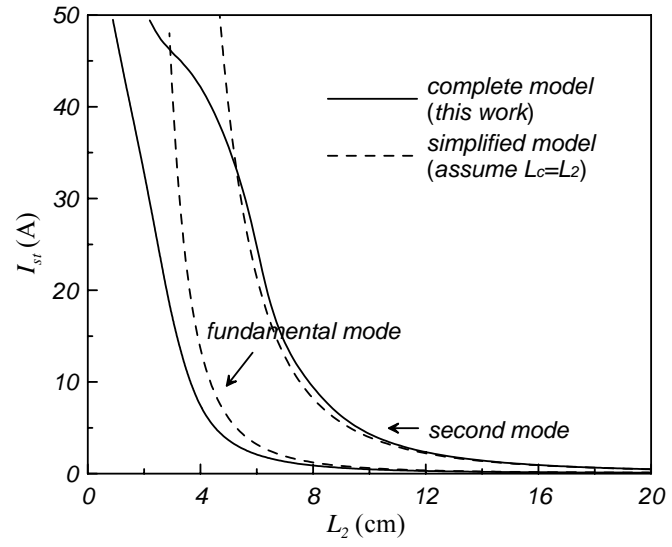


Fig. 9